

Original citation:

Chen, Chang-Hui, Jacobse, Leon, McKelvey, Kim M. (Kim Martin), Lai, Stanley C. S., Koper, Marc T. M. and Unwin, Patrick R.. (2015) Voltammetric scanning electrochemical cell microscopy : dynamic imaging of hydrazine electro-oxidation on platinum electrodes. *Analytical Chemistry*

Permanent WRAP url:

<http://wrap.warwick.ac.uk/67791>

Copyright and reuse:

The Warwick Research Archive Portal (WRAP) makes this work of researchers of the University of Warwick available open access under the following conditions. Copyright © and all moral rights to the version of the paper presented here belong to the individual author(s) and/or other copyright owners. To the extent reasonable and practicable the material made available in WRAP has been checked for eligibility before being made available.

Copies of full items can be used for personal research or study, educational, or not-for-profit purposes without prior permission or charge. Provided that the authors, title and full bibliographic details are credited, a hyperlink and/or URL is given for the original metadata page and the content is not changed in any way.

Publisher's statement:

This document is the Accepted Manuscript version of a Published Work that appeared in final form in *Analytical Chemistry* copyright © American Chemical Society after peer review and technical editing by the publisher. To access the final edited and published work see link to Published Work,

<http://pubs.acs.org/page/policy/articlesonrequest/index.html>]

The version presented here may differ from the published version or, version of record, if you wish to cite this item you are advised to consult the publisher's version. Please see the 'permanent WRAP url' above for details on accessing the published version and note that access may require a subscription.

For more information, please contact the WRAP Team at: publications@warwick.ac.uk

warwick**publications**wrap
highlight your research

<http://wrap.warwick.ac.uk/>

Voltammetric scanning electrochemical cell microscopy: dynamic imaging of hydrazine electro-oxidation on platinum electrodes

Chang-Hui Chen^{†, §}, Leon Jacobse^{†, ‡}, Kim McKelvey[§], Stanley C. S. Lai[¶], Marc T. M. Koper[‡], and Patrick R. Unwin^{*, §}.

[§]Department of Chemistry, University of Warwick, Gibbet Hill Road, Coventry CV4 7AL, UK

[‡]Leiden Institute of Chemistry, Leiden University, P.O. Box 9502, 2300 RA Leiden, The Netherlands.

[¶]MESA+ Institute for Nanotechnology, University of Twente, PO Box 217, 7500 AE Enschede, The Netherlands

* To whom correspondence should be addressed: P.R.Unwin@warwick.ac.uk

Abstract:

Voltammetric scanning electrochemical cell microscopy (SECCM) incorporates cyclic voltammetry measurements in the SECCM imaging protocol, by recording electrochemical currents in a wide potential window at each pixel in a map. This provides much more information compared to traditional fixed potential imaging. Data can be represented as movies (hundreds of frames) of current (over a surface region) at a series of potentials and are highly revealing of subtle variations in electrode activity. Furthermore, by combining SECCM data with other forms of microscopy, e.g. scanning electron microscopy and electron backscatter diffraction data, it is possible to directly relate the current-voltage characteristics to spatial position and surface structure. In this work we use a ‘hopping mode’, where the SECCM pipet probe is translated towards the surface at a series of positions until meniscus contact. Small amounts of residue left on the surface, upon probe retraction, demark the precise area of each measurement. We use these techniques to study hydrazine oxidation on a polycrystalline platinum substrate in air and in a deaerated environment. In both cases, the detected faradaic current shows a structural dependence on the surface crystallographic orientation. Significantly, in the presence of oxygen (aerated solution) the electrochemical current decreases strongly for almost all grains (crystallographic orientations). The results highlight the flexibility of voltammetric SECCM for electrochemical imaging and present important implications for hydrazine electroanalysis.

Introduction

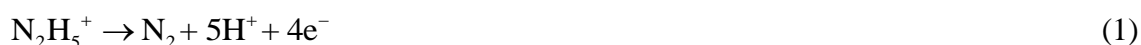
Electrochemical imaging is of interest for visualizing (electro)chemical processes at interfaces and provides valuable information about the associated kinetics, mass transport and localized activity. In traditional electrochemical imaging approaches, the electrochemical current is recorded at a fixed potential of interest and, typically, only one or a few images are recorded.¹⁻³ Dynamic imaging was reported by Wipf^{4,5} and Schuhmann⁶ by combining scanning electrochemical microscopy (SECM) with time-dependent techniques, such as cyclic voltammetry (CV) and potential pulse methods, although this type of approach has not been widely adopted and has not been used to gain information on heterogeneous electrode surface activity, having employed rather large probe electrodes.

Our group has been particularly interested in developing scanning electrochemical cell microscopy (SECCM) as a new way to reveal electrode surface activity, as demonstrated by a number of applications.⁷⁻¹¹ Recently, we have adopted a pseudo single-crystal approach, which combines SECCM and electron backscatter diffraction (EBSD), to study the structure-activity relationship at polycrystalline Pt, which comprises high index Pt facets and grain boundaries.^{12,13} However, so far, SECCM has been limited to imaging experiments at a few fixed potentials. In this paper, we describe voltammetric SECCM imaging, in a hopping mode, which combines CV and SECCM. A full CV is recorded at a number of locations (pixels) on the substrate, which are arranged in a (rectangular) grid. A wealth of information can be obtained from these measurements that can then be visualized in different ways (e.g. equipotential maps or spatially resolved CVs).

We focus on spatially-resolved studies of the electrocatalytic oxidation of hydrazine on a polycrystalline Pt electrode, and compare these results to those obtained on traditional macro- and microscale electrodes. Hydrazine (N_2H_4) is of practical interest due to its wide

application in the fields of electroanalysis and electrocatalysis. Liquid hydrazine is easily transferred and its oxidation offers relatively high power density with carbon-free products, making it a promising fuel for low temperature fuel cells.¹⁴⁻¹⁶ Hydrazine is also important in the pharmaceutical industry, as a common starting material in the synthesis of many pharmaceutical compounds.^{17,18} However, it is often a key impurity in pharmaceutical products, and its high toxicity has led to the development of (electrochemical) hydrazine sensors.¹⁹⁻²¹ Voltammetric and amperometric hydrazine analysis is usually performed in air and the role of oxygen in hydrazine detection is rarely taken into account.²² This is an important consideration, because hydrazine can (catalytically) reduce oxygen on various surfaces, a process that is exploited for corrosion protection.²³⁻²⁶ Thus, the faradaic response for hydrazine electro-oxidation (especially at trace levels) might be expected to change in the presence of O₂ in a manner that depends on the electrode structure, as we consider herein.

Pt and Pt-based electrodes are relatively active for hydrazine electro-oxidation and the mechanism and kinetics of hydrazine oxidation on Pt have received attention.²⁷⁻²⁹ The overall reaction oxidizes hydrazine to molecular nitrogen and depends on the pH of the solution:



Various possible intermediates and (pH-dependent) reaction pathways have been proposed. In general, no oxygen-containing compounds are detected by on-line electrochemical mass spectrometry (OLEMS)²⁸ and the N-N bond is found to remain intact through isotopic labelling.³⁰ As this is a catalytic reaction, the role of surface structure is of interest and has been investigated using Pt single-crystal electrodes.³¹⁻³³ For Pt in a weakly adsorbing electrolyte (perchloric acid), the reactivity (in terms of peak potential) for the basal planes decreases in the order of Pt(100) > Pt(111) > Pt(110).³² While single crystal research provides valuable information for basal planes, less is known about high index surfaces and grain

boundaries, of practical importance in polycrystalline or nanoparticle-based sensors, which is the focus of this paper.

In this work, voltammetric SECCM is used to study hydrazine oxidation at a polycrystalline platinum electrode in air and in a nitrogen atmosphere. Equipotential images and dynamic movies obtained from pixel-resolved CV measurements allow direct visualization of hydrazine oxidation across Pt surfaces at multiple different potentials and surface orientations. In the absence of oxygen, the structure-dependent reactivity of hydrazine oxidation for high-index surfaces is established. In air, the electrochemical current for hydrazine oxidation was found to decrease dramatically for most Pt facets, with important implications for hydrazine electroanalysis.

Experimental

Fresh electrolyte solutions were prepared before each experiment from ultra-pure water (SELECT-HP, Purite, 18.2 M Ω cm resistivity at 25 °C), HClO₄ (ca. 70 % solution in water, Acros Organics) and hydrazine monohydrate (Acros Organics). Pd-H₂ was used as a quasi-reference counter electrode (QRCE) for SECCM and as a reference electrode (RE) for macroscale and microscale experiments. This was prepared by evolving hydrogen on a Pd wire (99.9 % purity, 0.25 mm thickness; Alfa Aesar) in a supporting electrolyte (0.1 M HClO₄) solution. All reported potentials are against the reversible hydrogen electrode ($E_{\text{Pd-H}_2}^0 = 50 \text{ mV vs. RHE}$).³⁴

Macroscopic CV measurements were carried out in a traditional 3-electrode setup. A polycrystalline Pt wire was used as the working electrode, with the Pd-H₂ RE and another Pt wire as the counter electrode. Prior to each experiment these Pt electrodes were cleaned by flame-annealing. The exposed surface area of the working electrode was on the order of a few tens of mm² and varied somewhat between different experiments. No attempt was made to

determine the exact area as the hydrogen UPD region of the CV contains oxygen reduction reaction (ORR) features for the experiments performed in the presence of oxygen.

A 25 μm diameter Pt-disk ultramicroelectrode (UME) was prepared by sealing a Pt microwire into glass.³⁵ It was then polished on a 0.1 μm diamond-lapping disc (PSA, Buehler) until a flat surface was obtained. Before use, the Pt UME was cleaned by further mechanical polishing (MasterPrep 0.05 μm alumina polishing suspension, Buehler) and finally through the use of a clean polishing pad without alumina, followed by thorough rinsing with ultra-pure water. For experiments under deaerated conditions, the electrolyte solution (10 mL) was flushed with N_2 for 30 minutes before the measurements.

A polycrystalline Pt foil (> 99.95 % purity, 0.010 mm thickness; Advent Research Materials) was used as the substrate (working) electrode for the SECCM imaging experiments. Prior to each experiment, the foil was cleaned by rinsing with ultra-pure water and flame-annealing. An area of interest on the foil was marked by focused ion beam milling (JEOL 4500, JEOL). Scanning electron microscopy (SEM) images of the Pt substrate were recorded after each imaging experiment on a Zeiss SUPRA 55 variable-pressure field emission-scanning electron microscope. Electrolyte residues from the SECCM meniscus in the hopping mode employed (*vide infra*) were observed with SEM and provide valuable information about the exact droplet size and measurement location. Before each new experiment, all residues from any previous imaging were cleaned by immersing the foil in a diluted H_2SO_4 solution overnight.

The setup for voltammetric SECCM is illustrated in Figure 1. Briefly, a dual barrel pipet with a small opening (in this study ~ 1 μm diameter) was used to make a series of voltammetric measurements across an area of interest on the Pt substrate. The meniscus at the end of the pipet forms an electrochemical cell with the substrate and thus defines the working electrode area at each pixel. A bias voltage (V_1 , in this study 200 mV or 500 mV) was applied

between two Pd-H₂ quasi-reference counter electrodes (QRCEs, one in each barrel) to generate an ion conductance current (i_{DC}) between the barrels. The working electrode potential (E_s) is determined by both V_1 and a voltage (V_2) applied to one of the QRCEs, $E_s = -(V_2 + 0.5 \cdot V_1)$; Figure 1a. Modulation of the z-position of the tip (66 Hz or 266 Hz, 25-50 nm peak amplitude) produces an AC component in the ion conductance current (i_{AC}). A constant tip-to-substrate distance was maintained by using the magnitude of i_{AC} as feedback.⁷⁻

13

In previous SECCM and related studies, the substrate was scanned by the probe using a continuous scanning¹³ (for flat substrates) or approach-hold-withdraw (hopping) mode (for rough substrates and/or dissolution studies),^{36,37} while the substrate, if a conductor, was held at a constant potential (E_s). To directly extract data for a wide potential range, this latter hopping mode SECCM was combined with a potential sweep at each position, with the associated current response measured. Figure 1b illustrates the tip-to-substrate separation, as a function of time, t , during imaging, together with the corresponding potential-time profile applied to the substrate working electrode. The complete scanning process consisted of the following steps: slow approach of the pipet ($0.5 \mu\text{m s}^{-1}$); once in meniscus contact, the pipet position was held for 1 s to allow the droplet to stabilize; a potential sweep (0.1 V s^{-1}) to obtain the CV was then applied; quick retraction ($2.0 \mu\text{m s}^{-1}$) of the pipet far enough to break the meniscus; and movement in the xy -plane to repeat the process for the next pixel. For the CV measurement, current data were recorded at least every 1 mV, so that potentiodynamic movies containing many hundreds of frames could be produced.

The distance between adjacent pixels (2-3 μm) was chosen such that there was no overlap between each probed area (diameter $\sim 1 \mu\text{m}$). Another important factor to determine the pixel spacing was the total imaging time which was typically several hours. The retract distance was chosen based on the tip size and the roughness/flatness of the substrate and was

typically 1-1.5 μm . As a ‘fresh’ surface (*i.e.* a region of the surface that had not yet been in contact with the electrolyte solution) was encountered for each pixel, all CVs recorded in the SECCM imaging are the first CV at that particular position. SECCM experiments in deaerated conditions were carried out in an environmental cell, which was placed over the Pt foil and the pipet and was flushed with humidified N_2 (through a vial containing water) before starting the experiment and during imaging. Data analysis was performed in Matlab (R2014b, Mathworks). For the SECCM images shown in this paper, a two dimensional linear interpolation was applied to the data to guide the eye. This was reasonable as in most grains the current was fairly uniform across the grain.

EBSD images of the polycrystalline Pt substrate, in the same area of the SECCM measurements, were recorded on a Zeiss SUPRA 55 FE-SEM equipped with an EDAX TSL EBSD system. Before performing EBSD measurements, the Pt foil was cleaned carefully. The measurements were carried out at 20 kV at a working distance of 25 mm on a substrate tilted at 70° , with a data collection step of 2.5 μm . Data analysis was performed using Orientation Imaging Microscopy software.

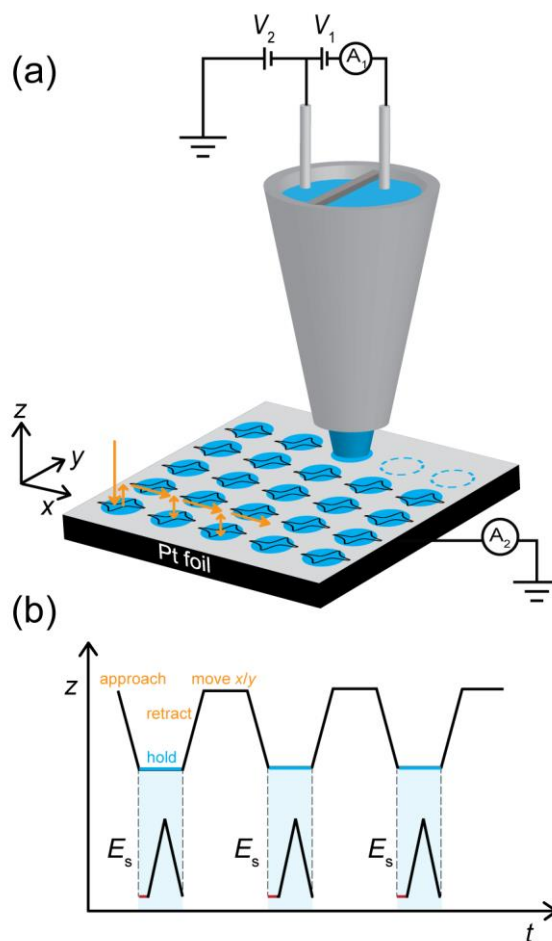


Figure 1. a) Schematic overview of the voltammetric hopping SECCM mode. V_1 and V_2 are the bias voltage and substrate voltage applied to one of the QRCEs, respectively. A_1 and A_2 are current amplifiers to measure i_{DC} and the substrate working electrode current (i_s), respectively. The blue circles indicate the probed areas of the working electrode and the arrows indicate the movement of the pipet. b) Schematic profiles of pipet-to-substrate separation (top) and the corresponding potential profile (bottom) applied to the substrate with time. The red lines in the potential profile indicate the hold time before recording a CV, typically 1s.

Results and discussion

Voltammetry of hydrazine oxidation at Pt electrodes

To study the electrochemistry of hydrazine and provide a comparison for the SECCM results, CV measurements were carried out at polycrystalline platinum electrodes at different scales. Typical CVs for hydrazine oxidation recorded on a mm-scale platinum wire, on a Pt UME, and on a polycrystalline Pt foil using a 1 μm diameter SECCM pipet are shown in

Figure 2. All CVs were recorded in a deaerated solution of 2 mM N_2H_4 in 0.1 M HClO_4 at 100 mV s^{-1} .

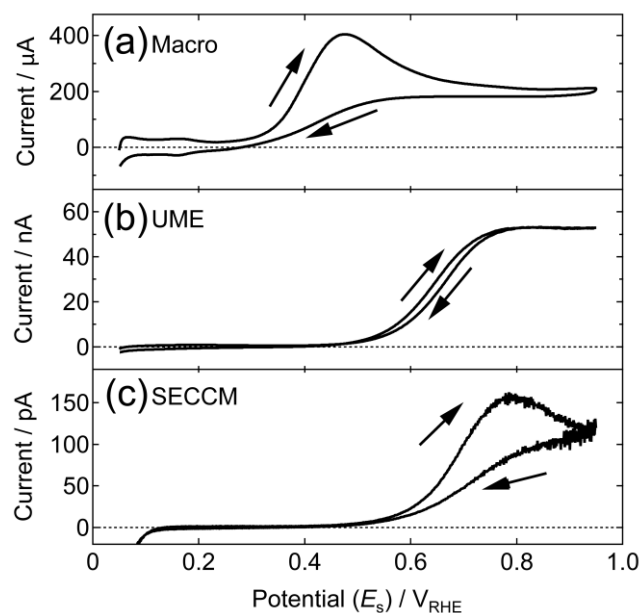


Figure 2. Typical CVs of hydrazine oxidation at a) a Pt wire, b) a 25 μm diameter Pt UME, and c) a polycrystalline Pt foil in a SECCM setup. Note the different current scales. In all cases the CVs were recorded in deaerated electrolyte solutions containing 2 mM N_2H_4 and 0.1 M HClO_4 . The sweep rates were 100 mV s^{-1} .

At the macroscopic Pt electrode, hydrazine oxidation in an acidic electrolyte starts just after the hydrogen desorption region and then quickly reaches peak current at ca. 0.48 V. In the case of the UME, (diffusional) mass transport is much faster than for the macroelectrode. In competition with the surface kinetics for hydrazine electro-oxidation this leads to an apparent shift in the onset potential to ca. 0.45 V. A steady-state current is observed at potentials above 0.80 V. Similar with CVs reported in literature, hydrazine oxidation is a reasonably facile process at both the macro- and the micro- scale, leading to mass transport limited reactivity at intermediate overpotentials.^{29,38} Figure 2c shows a typical CV for hydrazine oxidation at a platinum foil recorded in the SECCM setup. The oxidation of hydrazine has a similar onset potential as on the UME, but there is a small transient peak in the current at 0.80 V before a steady-state at more anodic potentials. Importantly, Figure 2c shows no features due to

oxygen reduction (which would be manifested in observable reduction currents well above the present cathodic onset of ~ 0.1 V), confirming the performance of the environmental cell, as the fast diffusion of O_2 from the surroundings across the meniscus to the surface would lead to a noticeable current.¹³ Furthermore, as we will show below, the presence of oxygen leads to significantly distorted features in the voltammetric profile for the oxidation of hydrazine.

The diffusion coefficient (D) calculated from the UME experiments ($i_{lim} = 4nFDcr^{39}$, where n is the number of electrons transferred per hydrazine molecule ($n = 4$), F is the Faraday constant, c is the bulk hydrazine concentration and r is the UME radius) is $1.4 \times 10^{-5} \text{ cm}^2 \text{ s}^{-1}$, and is consistent with values reported in the literature.^{40,41} In SECCM, the steady-state diffusion-limited current, i_{lim} , beyond the peak is 100 pA. The calculated mean mass transport coefficient, k_t ($k_t = i_{lim}/nFAc$, where A is the meniscus footprint area for 1 μm diameter spot size), in SECCM is $1.65 \times 10^{-2} \text{ cm s}^{-1}$. It is about 5 % of that for an inlaid UME ($k_t = 4D/\pi r$) of the same size, which is within the typical range reported for a micrometer-sized SECCM pipet,⁹ and similar to that of the 12.5 μm diameter UME. That the SECCM voltammogram shows a slight transient response compared to the UME (Figure 2b and c) is because of a very different current distribution in SECCM. For $N_2H_5^+$, which is the predominant species herein, there is a large difference in mass transport rate down the two channels of the theta pipet in SECCM.⁹ Further, note that some of the differences between the CVs in Figure 2 will be due to the different electrodes used, and methods of preparation, because as we show herein hydrazine oxidation is very surface sensitive.

In some recent work, a significant ‘activation’ of a Pt UME after scanning towards high oxidative potentials was reported, attributed to the formation of catalytic residual surface oxides in sequential voltammetric scans.³⁸ Several SECCM CVs were recorded in this study where the potential was scanned up to 1.45 V (see Supporting Information, section S1).

While there are small changes in the voltammetric signature, the responses were generally similar to the ‘stabilized’ CV reported³⁸ without the need of any initial activating scan. It should be kept in mind however, that our surface preparation is an oxidative process (flame-annealing), which could introduce such residual oxides. Nonetheless, to avoid possible complications due to further extensive Pt oxide formation and reduction, all the CVs in SECCM imaging experiments were recorded from 0.05 V to 0.95 V, focusing on the main response.

Voltammetric SECCM Imaging in deaerated environment

Figure 3a shows an EBSD image of a typical probed area of polycrystalline platinum foil. In this case SECCM focused on a $41\ \mu\text{m} \times 86\ \mu\text{m}$ area, with data recorded every $3\ \mu\text{m}$ within this area. We focus on the voltammetry of the four numbered grains as they present the limiting cases of the orientations present. EBSD results show that all the grains are high-index surfaces, but grain 1 and 3 have orientations approaching (111), while grain 2 has an orientation approaching (100). Grain 4 lies in between (100) and (110).

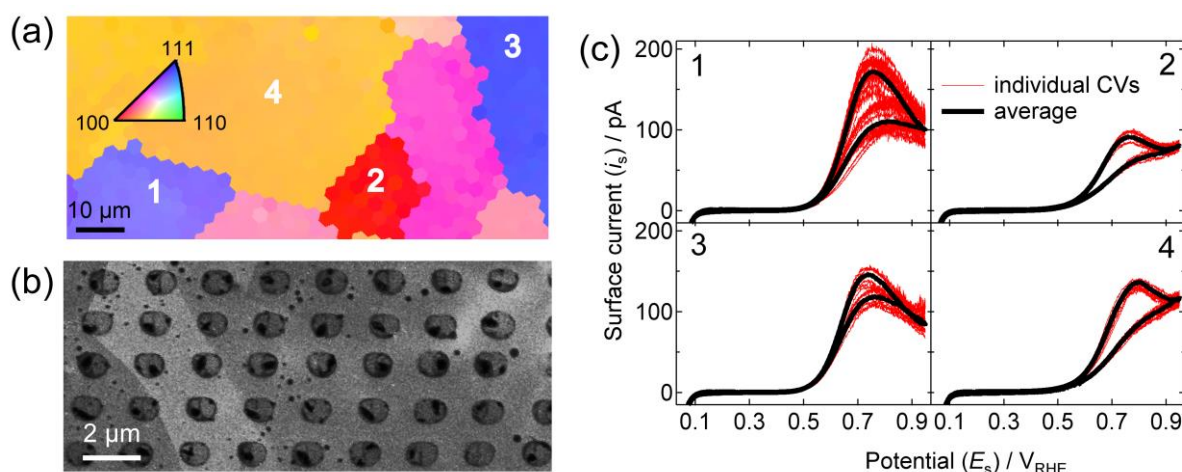


Figure 3. a) EBSD image of the Pt foil used in the SECCM imaging experiments. The grain orientations are indicated in the triangle; b) a typical SEM image of a part of a scanned area after SECCM imaging. c) Individual CVs (red, 7-10 for each grain) and grain-averaged CVs (black) for different grains.

Optical microscopy and SEM images after SECCM imaging showed droplet residues on the surface due to the quick breaking of the meniscus during probe retraction. Figure 3b is a typical zoomed-in SEM image after an SECCM measurement. These droplet residues are fairly consistent in shape and size at the different grains, confirming the stability and reproducibility of the technique and the absence of a dependence of droplet wetting on the surface structure. Additionally, the residues helped us to determine the exact scanned area and droplet size (meniscus footprint) after SECCM imaging.

By combining the results from SECCM, SEM, and EBSD, the position of each individual CV can be determined. Figure 3c shows CVs from 7-10 pixels obtained on each of the four numbered grains. On top of the individual CVs, an averaged CV is plotted for each grain to show the representative CV feature of that area. It is clear that the variation within a particular grain is fairly small, particularly for grain 2 and grain 4, but the character of the grain has a significant impact on the voltammetric response. This is not due to changes in the meniscus contact area as the footprint is reasonably consistent, as pointed out above, and shown over a more extensive region in Supporting Information, Section S2 (Figure S-2). Moreover, the corresponding i_{DC} images (Supporting Information, Movie S3) show no structural dependent features. Although all the grains are high index surfaces, grains 1 and 3, which have contributions mainly from the (111) orientation, have very similar CVs. Grains 2 and 4, which are mainly (100) oriented, show lower peak currents and higher peak potentials. Furthermore, closer inspection reveals that on grains 1 and 3 (mainly of (111) orientation), the current decrease after the peak is reversible (increasing again after reversal of the potential sweep direction). This is likely related to the initial stages of surface oxide formation on Pt(111) in perchloric acid, which is highly reversible.⁴² In contrast, on grains 2 and 4 (mainly (100) orientation), the current continues to decrease after reversal of the sweep

direction, mirroring the irreversibility of surface oxidation on Pt(100).⁴² Thus, we believe surface oxidation/reduction kinetics is (one of) the factors determining the shape of the voltammogram. Significantly, this effect would have remained unnoticed in (conventional) fixed-potential imaging, highlighting a considerable strength of voltammetric scanning SECCM. Importantly, these results illustrate that hydrazine oxidation at high index Pt surfaces is strongly structure dependent.

In addition to individual and averaged CVs, the spatially resolved reactivity can be visualized through activity maps of various types. For example, as current values were recorded at least every 1 mV during the pixel-resolved CV measurements, we can construct a series of equipotential maps by plotting the electrochemical activity current (i_s) of all pixels at a given potential as a function of spatial position. The full series can then be compiled as a movie as shown in Supporting Information (Movie S4), which illustrates the localised evolution of the surface current during a cyclic potential sweep. In the movie, with increasing potential, the activity of different grains starts to show up, providing a direct view of the electrochemical activity across the surface. Figures 4a and 4b are two frames of data from the i_s movie during the forward scan at potentials of 0.60 V and 0.78 V respectively, but with the color scales adjusted to highlight the full current range at each potential. These maps are conceptually similar to maps which could have been obtained with fixed potential SECCM imaging, but with our approach these are 2 maps of 1800 maps that can be constructed from the data at different potentials. The chosen potentials for Figures 4a and 4b are close to the onset of the oxidation current (Figure 4a, $E_s = 0.60$ V) and the peak potential (Figure 4b, $E_s = 0.78$ V). In Figure 4a, grains 1 and 3 can be recognized as having higher activity, while grains 2 and 4 are visible in Figure 4b.

As evident in Figure 3c, SECCM CVs on this time scale typically show a peak during the oxidative potential sweep, and the potential at which this peak occurs is related semi-

quantitatively to the driving force required for the reaction. This is shown in Figure 4c, from which it is clear that the peak occurs at lower overpotential, the higher the current in the surface activity maps in Figure 4a and 4b. Using another approach, a high order polynomial was fitted through each pixel-resolved CV to calculate $\partial i/\partial E_s$, with the result at $E_s = 0.75$ V shown in Figure 4d. This quantity again gives a measure of the ease of reaction, and the result is a map showing the distinct behaviour of the different grains. Finally, Tafel analysis was performed for all four grains, using the potential interval from 0.45 V to 0.65 V (at the foot of the wave, where mass transport and concentration polarization can be neglected) and is shown in Figure 4e. For the whole area, the Tafel slope is mainly within the range of 80 to 140 mV per decade. This range is within that of the previously reported Tafel slope values, 82 mV per decade to 110 mV per decade, for polycrystalline Pt electrodes in acidic solution.^{29,43} However, our data are very illuminating showing that the precise slope is very grain-orientation dependent. The average Tafel slopes for grains from 1 to 4 are 100 ± 12 , 130 ± 2 , 88 ± 3 and 139 ± 3 mV per decade, respectively. Comparing Figure 4a-b to 4c-e, it is demonstrated through the use of voltammetric SECCM it becomes possible to visualize/identify differences (especially in the $\partial i/\partial E_s$ maps) in electrochemical activity which would be invisible using fixed potential imaging.

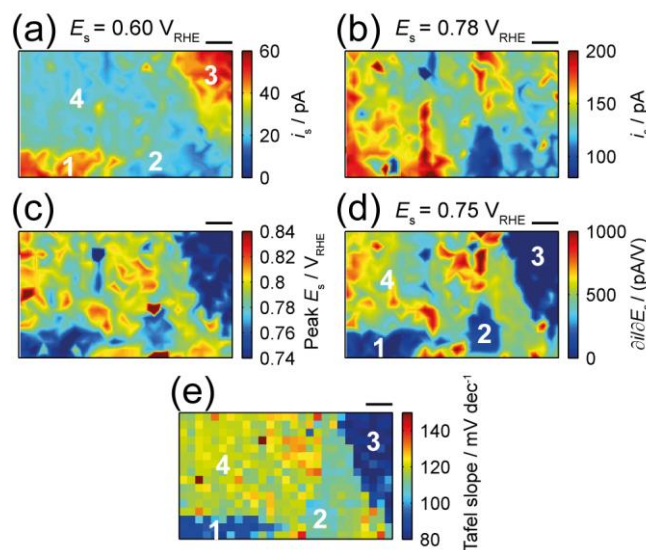


Figure 4. Various map representations of the SECCM data; a-b) activity, expressed as substrate current maps for $E_s = 0.60$ V and 0.78 V; c) peak potential; d) $\partial i/\partial E_s$ at $E_s = 0.75$ V. Note the different color scales. e) Tafel slope in mV per decade determined using the data from $0.45 > E_s > 0.65$ V. The scale bar is $10\text{ }\mu\text{m}$ in all images.

Voltammetric SECCM of hydrazine oxidation in air

Besides the faradaic oxidation of hydrazine, there are also studies reporting catalytic (non-faradaic) decomposition of hydrazine.^{25,44} Although the non-faradaic oxidation of hydrazine in air is slow at room temperature, it can be accelerated in the presence of catalysts, such as platinum, copper, and manganese.^{25,30,44} As we have demonstrated recently that the three phase boundary in SECCM¹³ provides high mass transport of oxygen, SECCM is an interesting technique to study the role of O_2 in the total oxidation reaction. Thus, imaging experiments were performed in the same area as shown in Figure 3a, but on a newly cleaned surface, without using the environmental cell. CVs were recorded every $2\text{ }\mu\text{m}$ between 0.45 V and 0.95 V.

Figure 5a shows an equipotential i_s map extracted from the SECCM imaging experiment in air, at 0.78 V. Movies of i_s and i_{DC} for the CV measurements are provided in the Supporting Information (Movie S5 and S6). Compared with Figure 3c, Figure 5a shows that except for grain 1, the electrochemical activity of all the grains is almost completely suppressed. Similar to the approach in Figure 3c, CVs recorded at grains 1 to 4 at single pixels (red) and the averaged ones (black) are shown in Figure 5b. It is clear that hydrazine oxidation CVs in air exhibit different shapes and much lower current values compared with CVs in the absence of O_2 , with the peak current, when discernible, shifted to higher overpotential.

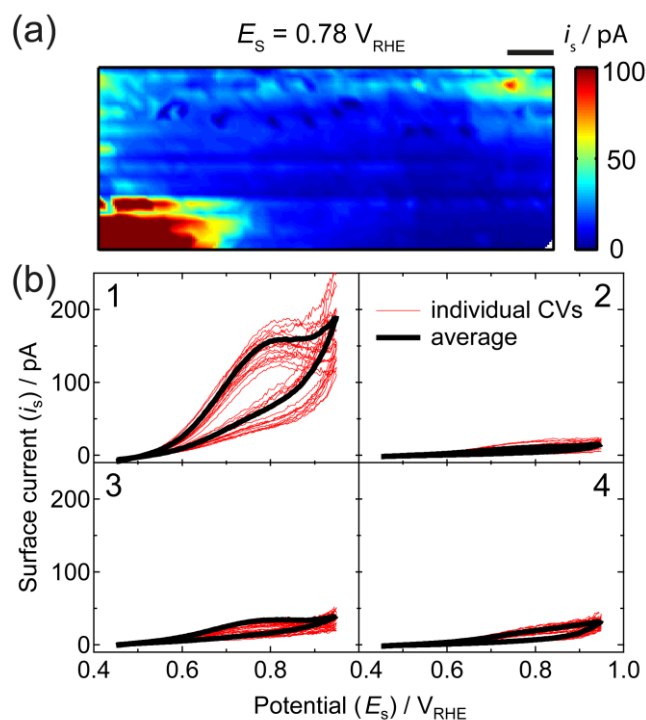


Figure 5. a) Equipotential i_s map of hydrazine oxidation in air at $E_s = 0.78$ V. The scale bar is 10 μm . b) Individual (red, 10-20 for each grain) and averaged (black) CVs for different grains in air. Numbers in b) correspond to grain areas marked in Figure 3a.

To further understand the role of oxygen and the cause of the large differences in activity, a blank SECCM experiment in air was performed using just the supporting electrolyte. The potential was scanned between 0.45 V and 1.35 V at a sweep rate of 0.5 V s^{-1} . Averaged CVs in each of the four grains for all three imaging experiments (hydrazine oxidation in a deaerated solution, hydrazine oxidation in the presence of dissolved oxygen and blank CVs) are summarized in Figure 6. Comparing the three measurements, it is clear that, generally, the presence of oxygen leads to a decrease in the currents observed for the oxidation of hydrazine. There are two main causes of this effect. First, it can be seen in the blank CVs that at potentials below 0.65 V, there is a significant (reduction) current due to the ORR, in agreement with our previous findings.¹³ Thus, at potentials between 0.45 V and 0.65 V, the oxidation of hydrazine (positive current) overlaps with the reduction of oxygen (negative current) in aerated solution, and the overall observed current in this potential range represents

the sum of the two processes. As a result, the apparent current for the oxidation of hydrazine in air in this potential range is much smaller than that of the oxidation of hydrazine in deaerated conditions (and, similarly, the reduction current of oxygen with hydrazine present is smaller (in absolute terms) than that of the reduction of oxygen in the absence of hydrazine). Second, as mentioned above, hydrazine can react with oxygen through the following reaction at a catalyst (such as platinum) surface:



This non-faradaic (*i.e.* no ‘current-producing’) reaction consumes hydrazine, thereby lowering the interfacial concentration of hydrazine. In fact, this reaction is most likely exacerbated in our experimental setup, as is the ORR effect mentioned above, due to the enhanced mass transport of oxygen at the three-phase boundary.¹³ Consequently, a lower current for the (electrochemical) oxidation of hydrazine is observed compared to a deaerated solution, as the current is directly proportional hydrazine concentration.

In fact, we can exploit this second mechanism to obtain the structural dependency (at least in a semi-quantitative manner) of the non-faradaic reaction between oxygen and hydrazine. By using the observed current in the presence of oxygen as a probe for the residual hydrazine concentration (that is, the hydrazine concentration after the non-faradaic consumption of hydrazine), we can deduce the extent to which the non-faradaic reaction takes place. Specifically, substrate regions where there is a small decrease in current (such as grain 1) indicate a low activity towards the non-faradaic reaction, whereas a large decrease (such as grains 2, 3 and 4) represents a high activity. Using this approach, we find the activity towards the non-faradaic reaction of hydrazine and oxygen to follow the relative order: grain 2 > grain 4 > grain 3 > grain 1. Interestingly, this is the inverse of the electrochemical activity (see Figure 3c), and, at least in part, this rationalizes the trend because the faradaic and non-faradaic processes are in competition. Importantly, these results provide a novel method to

probe local structure effects in non-faradaic catalytic reactions through electrochemical measurements, an avenue we will further explore in the future. There are also clearly implications for the optimal design of hydrazine voltammetric sensors in aerated solution.

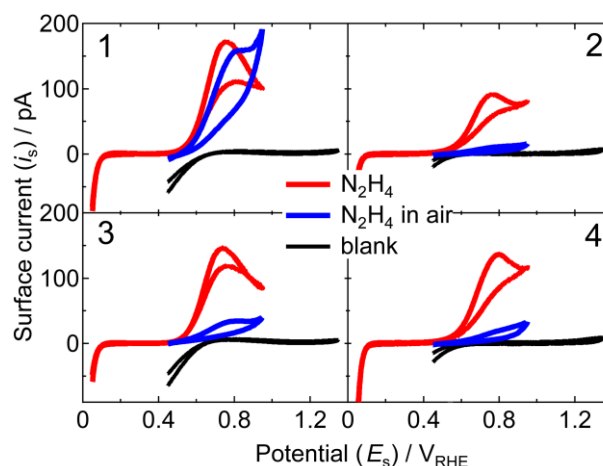


Figure 6. Comparison of N₂H₄ oxidation (red) in deaerated environment, N₂H₄ oxidation in air (blue), and blank (in air, black) averaged CVs for different grain orientations (numbers indicated).

Conclusions

In this contribution, we have highlighted the considerable power of voltammetric SECCM, which combines SECCM with CV measurements, as a methodology for electrochemical imaging. Compared to traditional fixed potential imaging,^{8,11,13,45} this approach has significant attributes. First, as CVs are recorded at every pixel of the scanned area, it is possible to probe local electrochemical currents at multiple potentials (1800 separate potentials in the deaerated hydrazine CVs herein) and thus increases imaging efficiency. Furthermore, as the meniscus breaks and droplet residues are left on the substrate, as the pipet moves to a new position on the substrate for the next measurement, it is possible to determine the exact position and surface area of each pixel. Finally, it allows for potentiodynamic information to be obtained, complementing potentiostatic information from fixed potential imaging, which both have their uses in certain situations (*cf.* cyclic voltammetry and chronoamperometry).

In this work, using voltammetric SECCM, we studied hydrazine oxidation at high-index Pt surfaces in air and in a deaerated environment. We found CV characteristics of hydrazine oxidation at Pt electrode are strongly surface structure dependent. The reactivity of hydrazine at different surfaces can be compared from equipotential maps and dynamic movies. For all grains studied here, grains having more (111) features show higher activity than grains having more (100) features. This might appear to counter studies with single crystal electrodes, but it should be noted that the studies herein are on high-index and high defect facets, highlighting the importance of such features in the electrocatalytic oxidation of hydrazine oxidation on practical surfaces.

Significant changes in hydrazine oxidation activity were observed in air, where oxygen transfers through the three-phase boundary of the SECCM with high rates. We found the presence of oxygen strongly decreased the detected electrochemical current for hydrazine oxidation at most of the Pt grains. The variation in activity between different grains was also much more pronounced than in the absence of air. We ascribe these changes to the overlap between the potentials for hydrazine oxidation and ORR as well as the non-faradaic decomposition of hydrazine with oxygen at certain Pt facets. These results emphasize the importance of considering oxygen in the voltammetric detection of hydrazine, which could greatly affect the response of the hydrazine sensors in a manner dependent on the Pt substrate used.

ACKNOWLEDGEMENTS

This project was supported by the European Union, through the European Research Council (Advanced Investigator Grant ERC-2009-AdG 247143; “QUANTIF”). The authors acknowledge a University of Warwick Chancellor’s International Scholarship award to C-HC. We thank Dr. Alex Colburn (University of Warwick) for his expert contributions on SECCM

instrumentation and custom electronics.

ASSOCIATED CONTENT

Supporting Information

S1. Cyclic voltammograms (CVs) of hydrazine oxidation at an ultramicroelectrode (UME) and in the SECCM setup

S2. Scanning electron microscopy (SEM) image of the Pt foil after voltammetric scanning electrochemical cell microscopy (SECCM) imaging

S3. Ion conductance current (i_{DC}) movie of hydrazine oxidation at deaerated conditions

S4. Electrochemical current (i_s) movie of hydrazine oxidation at deaerated conditions

S5. i_s movie of hydrazine oxidation in air

S6. i_{DC} movie of hydrazine oxidation in air

This material is available free of charge via the internet at <http://pubs.acs.org>.

AUTHOR INFORMATION

Corresponding Author

E-mail: P.R.Unwin@warwick.ac.uk

Author Contributions

[†]These authors have contributed equally.

REFERENCES

- (1) Bard, A. J.; Mirkin, M. V. *Scanning Electrochemical Microscopy*; Marcel Dekker: New York, 2001.
- (2) Bard, A. J.; Fan, F. R. F.; Kwak, J.; Lev, O. *Anal. Chem.* **1989**, *61*, 132-138.
- (3) Amemiya, S.; Bard, A. J.; Fan, F. R. F.; Mirkin, M. V.; Unwin, P. R. *Annu. Rev. Anal. Chem.* **2008**, *1*, 95-131.
- (4) Díaz-Ballote, L.; Alpuche-Aviles, M.; Wipf, D. O. *J. Electroanal. Chem.* **2007**, *604*, 17-25.
- (5) Schrock, D. S.; Wipf, D. O.; Baur, J. E. *Anal. Chem.* **2007**, *79*, 4931-4941.
- (6) Nebel, M.; Grützke, S.; Diab, N.; Schulte, A.; Schuhmann, W. *Faraday Discuss.* **2013**, *164*, 19-32.
- (7) Ebejer, N.; Schnippering, M.; Colburn, A. W.; Edwards, M. A.; Unwin, P. R. *Anal. Chem.* **2010**, *82*, 9141-9145.
- (8) Ebejer, N.; Güell, A. G.; Lai, S. C. S.; McKelvey, K.; Snowden, M. E.; Unwin, P. R. *Annu. Rev. Anal. Chem.* **2013**, *6*, 329-351.
- (9) Snowden, M. E.; Güell, A. G.; Lai, S. C. S.; McKelvey, K.; Ebejer, N.; O'Connell, M. A.; Colburn, A. W.; Unwin, P. R. *Anal. Chem.* **2012**, *84*, 2483-2491.

- (10) Lai, S. C. S.; Patel, A. N.; McKelvey, K.; Unwin, P. R. *Angew. Chem. Int. Ed.* **2012**, *51*, 5405-5408.
- (11) Güell, A. G.; Ebejer, N.; Snowden, M. E.; Macpherson, J. V.; Unwin, P. R. *J. Am. Chem. Soc.* **2012**, *134*, 7258-7261.
- (12) Aaronson, B. D. B.; Chen, C.-H.; Li, H.; Koper, M. T. M.; Lai, S. C. S.; Unwin, P. R. *J. Am. Chem. Soc.* **2013**, *135*, 3873-3880.
- (13) Chen, C.-H.; Meadows, K. E.; Cuharuc, A.; Lai, S. C. S.; Unwin, P. R. *Phys. Chem. Chem. Phys.* **2014**, *16*, 18545-18552.
- (14) Serov, A.; Kwak, C. *Appl. Catal., B* **2010**, *98*, 1-9.
- (15) Yamada, K.; Asazawa, K.; Yasuda, K.; Ioroi, T.; Tanaka, H.; Miyazaki, Y.; Kobayashi, T. *J. Power Sources* **2003**, *115*, 236-242.
- (16) Rees, N. V.; Compton, R. G. *Energy Environ. Sci.* **2011**, *4*, 1255-1260.
- (17) Elder, D. P.; Snodin, D.; Teasdale, A. J. *J. Pharm. Biomed. Anal.* **2011**, *54*, 900-910.
- (18) Liu, D. Q.; Sun, M.; Kord, A. S. J. *J. Pharm. Biomed. Anal.* **2010**, *51*, 999-1014.
- (19) Metters, J. P.; Tan, F.; Kadara, R. O.; Banks, C. E. *Anal. Methods* **2012**, *4*, 1272.
- (20) Liu, J.; Li, Y.; Jiang, J.; Huang, X. *Dalton Trans.* **2010**, *39*, 8693-8697.
- (21) Chakraborty, S.; Raj, C. R. *Sens. Actuators, B* **2010**, *147*, 222-227.
- (22) Hu, G.; Zhou, Z.; Guo, Y.; Hou, H.; Shao, S. *Electrochem. Commun.* **2010**, *12*, 422-426.
- (23) Moussa, M.; Taha, F.; Gouda, M.; Singab, G. *Corros. Sci.* **1976**, *16*, 379-385.
- (24) Andries, V.; Couturier, D. *Mater. Perform.* **2000**, *39*, 58-61.
- (25) Cuy, E.; Bray, W. J. *Am. Chem. Soc.* **1924**, *46*, 1786-1795.
- (26) Moon, J.-S.; Park, K.-K.; Kim, J.-H.; Seo, G. *Appl. Catal., A* **1999**, *184*, 41-48.
- (27) Bard, A. J. *Anal. Chem.* **1963**, *35*, 1602-1607.
- (28) Rosca, V.; Koper, M. T. M. *Electrochim. Acta* **2008**, *53*, 5199-5205.
- (29) García, M. D.; Marcos, M. L.; Velasco, J. G. *Electroanalysis* **1996**, *8*, 267-273.
- (30) Arnolds, K. Z. *Naturforsch., A: Phys., Phys. Chem., Kosmophys.* **1974**, *29*, 359-360.
- (31) Nishihara, C.; Raspini, I. A.; Kondoh, H.; Shindo, H.; Kaise, M.; Nozoye, H. *J. Electroanal. Chem.* **1992**, *338*, 299-316.
- (32) Álvarez-Ruiz, B.; Gómez, R.; Orts, J. M.; Feliu, J. M. *J. Electrochem. Soc.* **2002**, *149*, D35-D45.
- (33) Gómez, R.; Orts, J. M.; Rodes, A.; Feliu, J. M.; Aldaz, A. J. *J. Electroanal. Chem.* **1993**, *358*, 287-305.
- (34) Vasile, M. J.; Enke, C. G. *J. Electrochem. Soc.* **1965**, *112*, 865-870.
- (35) Macpherson, J. V.; Unwin, P. R. *Anal. Chem.* **1997**, *69*, 2063-2069.
- (36) Kinnear, S. L.; McKelvey, K.; Snowden, M. E.; Peruffo, M.; Colburn, A. W.; Unwin, P. R. *Langmuir* **2013**, *29*, 15565-15572.
- (37) Edwards, M. A.; Williams, C. G.; Whitworth, A. L.; Unwin, P. R. *Anal. Chem.* **2009**, *81*, 4482-4492.
- (38) Aldous, L.; Compton, R. G. *Phys. Chem. Chem. Phys.* **2011**, *13*, 5279-5287.
- (39) Saito, Y. *Review of Polarography* **1968**, *15*, 177-187.
- (40) Dudin, P. V.; Unwin, P. R.; Macpherson, J. V. *Phys. Chem. Chem. Phys.* **2011**, *13*, 17146-17152.
- (41) Eisner, U.; Gileadi, E. *J. Electroanal. Chem. Interfacial Electrochem.* **1970**, *28*, 81-92.
- (42) Rodes, A.; Zamakhchari, M. A.; El Achi, K.; Clavilier, J. J. *J. Electroanal. Chem. Interfacial Electrochem.* **1991**, *305*, 115-129.
- (43) Harrison, J. A.; Khan, Z. A. *J. Electroanal. Chem. Interfacial Electrochem.* **1970**, *28*, 131-138.
- (44) Gaunt, H.; Wetton, E. A. M. *J. Appl. Chem.* **1966**, *16*, 171-176.
- (45) Lai, S. C. S.; Dudin, P. V.; Macpherson, J. V.; Unwin, P. R. *J. Am. Chem. Soc.* **2011**, *133*, 10744-10747.

TABLE OF CONTENTS GRAPHIC

